remote sensing

MDPI

Article

Identifying the Spatial Heterogeneity and Driving Factors of Satellite-Based and Hydrologically Modeled Profile Soil Moisture

Han Yang [1,2,*], Xiaoqi Zhang [1], Zhe Yuan [1], Bin Xu [1] and Junjun Huo [1]

[1] Hubei Key Laboratory of Water Resources & Eco-Environmental Sciences, Changjiang River Scientific Research Institute, Wuhan 430010, China
[2] State Key Laboratory of Water Resources and Hydropower Engineering Science, Wuhan University, Wuhan 430072, China
* Correspondence: yanghan@mail.crsri.cn; Tel.: +86-15308626102

Abstract: Profile soil moisture (PSM), the soil water content in the whole soil layer, directly controls the major processes related to biological interaction, vegetation growth, and runoff generation. Its spatial heterogeneity, which refers to the uneven distribution and complexity in space, influences refined spatial management and decision-making in ecological, agricultural, and hydrological systems. Satellite instruments and hydrological models are two important sources of spatial information on PSM, but there is still a gap in understanding their potential mechanisms that affect spatial heterogeneity. This study is designed to identify the spatial heterogeneity and the driving factors of two PSM datasets; one is preprocessed from a satellite product (European Space Agency Climate Change Initiative, ESA CCI), and the other is simulated from a distributed hydrological model (the DEM-based distributed rainfall-runoff model, DDRM). Three catchments with different climate conditions were chosen as the study area. By considering the scale dependence of spatial heterogeneity, the profile saturation degree (PSD) datasets from different sources (shown as ESA CCI PSD and DDRM PSD, respectively) during 2017 that are matched in terms of spatial scale and physical properties were acquired first based on the calibration data from 2014–2016, and then the spatial heterogeneity of the PSD from different sources was identified by using spatial statistical analysis and the semi-variogram method, followed by the geographic detector method, to investigate the driving factors. The results indicate that (1) ESA CCI and DDRM PSD are similar for seasonal changes and are overall consistent and locally different in terms of the spatial variations in catchment with different climate conditions; (2) based on spatial statistical analysis, the spatial heterogeneity of PSD reduces after spatial rescaling; at the same spatial scale, DDRM PSD shows higher spatial heterogeneity than ESA CCI PSD, and the low-flow period shows higher spatial heterogeneity than the high-flow period; (3) based on the semi-variogram method, both ESA CCI and DDRM PSD show strong spatial heterogeneity in most cases, in which the proportion of $C/(C_0 + C)$ is higher than 0.75, and the spatial data in the low-flow period mostly show larger spatial heterogeneity, in which the proportion is higher than 0.9; the spatial heterogeneity of PSD is higher in the semi-arid catchment; (4) the first three driving factors of the spatial heterogeneity of both ESA CCI and DDRM PSD are DEM, precipitation, and soil type in most cases, contributing more than 50% to spatial heterogeneity; (5) precipitation contributes most to ESA CCI PSD in the low-flow period, and there is no obvious high contribution of precipitation to DDRM PSD. The research provides insights into the spatial heterogeneity of PSM, which helps develop refined modeling and spatial management strategies for soil moisture in ecological, agricultural, and hydrological fields.

Keywords: ESA CCI SM products; distributed hydrological model; profile soil moisture; spatial heterogeneity

Citation: Yang, H.; Zhang, X.; Yuan, Z.; Xu, B.; Huo, J. Identifying the Spatial Heterogeneity and Driving Factors of Satellite-Based and Hydrologically Modeled Profile Soil Moisture. *Remote Sens.* **2024**, *16*, 448. https://doi.org/10.3390/rs16030448

Academic Editors: Uta Heiden, Nikolaos L. Tsakiridis and Nikolaos Tziolas

Received: 27 November 2023
Revised: 21 January 2024
Accepted: 22 January 2024
Published: 24 January 2024

1. Introduction

Profile soil moisture (PSM), which refers to the soil water content in the whole soil layer, is the key variable in ecological, agricultural, and hydrological systems since it controls the major processes related to biological interaction, vegetation growth, and runoff generation [1–3]. In recent years, abundant studies have been conducted to investigate the temporal change in PSM based on in situ soil moisture datasets or other long time-series soil moisture datasets, but less attention is paid to its spatial distribution during a specific time period [4–10]. The spatial heterogeneity of PSM, which refers to the uneven distribution and complexity of data in space, helps develop refined partitioned management strategies in ecological, agricultural, and hydrological fields. Thus, it is necessary to pay more attention to the spatial heterogeneity of PSM.

Currently, satellite instruments and hydrological models are widely used to acquire spatial information on soil moisture. In situ stations can provide the most accurate soil moisture observations but are sparse and expensive in most regions and represent only spotty patterns of soil moisture that lack representativeness in terms of areal information [11,12]. Various satellite instruments can remotely sense spatial distributions of land surface variables, such as brightness temperature, and these further provide soil moisture products based on retrieval algorithms [13–19]. However, satellite instruments can only provide spatial distribution information on surface soil moisture (SSM) since only surface soil conditions can be remotely sensed by satellites. Some organizations provide raw-satellite-data-based PSM datasets, which are acquired by assimilating the raw satellite SSM into land surface models or exponential filters [20,21]. Compared to the raw SSM products, these PSM products are used less since they lack validation in terms of regions. As for hydrological models, most of them have the ability to directly simulate PSM [2]. Some lumped hydrological models, such as the XAJ model, consider the spatial heterogeneity of PSM through water storage capacity distribution curves and other methods but cannot provide real spatial distribution information on soil moisture [22]. Distributed hydrological models have the ability to provide spatial-temporal distribution information on PSM at the model-designed temporal and spatial scales [23,24]. However, this spatial information from hydrological models is not directly observed; rather, it is indirectly simulated and is, thus, affected by uncertainties from input data, model structures, model parameters, etc.

Although satellite instruments and hydrological models have their own advantages and disadvantages in terms of providing the spatial distribution of PSM, both of them have the potential to be used for the identification of the spatial heterogeneity of PSM. It can be noticed that there are different potential mechanisms that influence the spatial patterns of the PSM acquired from these two sources. For satellite instruments, PSM is calculated based on the raw SSM products, and the raw SSM is calculated based on remote sensing optical factors, such as brightness temperature. The underlying processes that influence the spatial patterns of satellite-based PSM are related to spectral characteristics, which may be largely affected by terrain, vegetation cover, land use, etc. As for hydrological models, their PSM simulations are the simulated intermediate variables of rainfall-runoff transformations; they are more likely to follow the change of input meteorological conditions and are limited by hydrological conditions through model calibration. The underlying processes that influence the spatial patterns of the PSM simulations are hydrological processes, among which precipitation, evapotranspiration, and runoff may be the major influential factors. Overall, satellite-based and hydrologically modeled PSM have the ability to represent some of the information of a spatial pattern, but both of them have difficulty in representing the real spatial distribution of PSM.

In order to seek out the real spatial heterogeneity of PSM, this study was developed to identify the spatial heterogeneity of PSM from both satellite instruments and hydrological models and investigate the respective driving factors. In recent research, there is still a gap in terms of understanding their potential mechanisms and differences. Some studies analyze the spatial heterogeneity of soil moisture and its driving factors without specialized indicators to identify the spatial heterogeneity. Lei et al. (2018) assessed the impact of

spatial heterogeneity on microwave satellite soil moisture periodic error and found that there is a causal relationship between satellite soil moisture periodic error and the spatial heterogeneity of brightness temperature, land cover types, and long-term averaged vegetation indices [25]. Zhang et al. (2022) evaluated the effects of climate change and human activities on the spatial heterogeneity of soil moisture based on GLDAS-2.1 (Global Land Data Assimilation System-2.1) SM products in the Tibetan Plateau by using a geographic detector method [26]. There are also some papers that report using specialized indicators to identify the spatial heterogeneity of soil moisture. For instance, Yang et al. (2017) and Zhang et al. (2021) used a semi-variogram to identify the spatial heterogeneity of field sampling soil moisture [27,28]. These studies pay more attention to investigating the spatial heterogeneity of soil moisture from one source, but fewer studies consider the possible difference in spatial heterogeneity when data are acquired from different sources.

This study chose European Space Agency Climate Change Initiative (ESA CCI) soil moisture products and the distributed hydrological model (the DEM-based distributed rainfall-runoff model, DDRM) PSM simulations as sources and three catchments of different climate scenarios as the study area to investigate the spatial heterogeneity and the driving factors of satellite-based and hydrologically modeled PSM. When considering the scale dependence of spatial heterogeneity, the prerequisite for identifying and comparing the spatial heterogeneity of satellite-based and hydrologically modeled PSM is that the datasets are mutual and match. This study first acquired profile saturation degree (PSD) data from different sources that matched hydrologically modeled and satellite raw product preprocessing in terms of spatial scale and physical properties; then, we identified their spatial heterogeneity and driving factors by using spatial statistical characteristic analysis, a semi-variogram, and a geographic detector method. In the rest of the paper, the study area, remotely sensed data, and other data used in the study are presented in Section 2, followed by the method used to acquire matching PSM from different sources, as well as the method used to identify the spatial heterogeneity and its driving factors of PSM in Section 3. Sections 4 and 5 show the results and discussion, respectively, and Section 6 concludes the paper.

2. Study Area and Datasets

2.1. Study Area

The study chose two humid catchments and one semi-arid catchment as the study area, including the Qu River (QR) catchment located in the upper and middle reaches of the Yangtze River, the Nanpan River (NR) catchment located in the upper reaches of the Xi River, which is one of the Pearl River tributaries, and the Yiluo River (YR) catchment located in the lower reaches of the Yellow River. The locations and the details of the chosen catchments are shown in Figure 1. The QR catchment has a drainage area of 39,211 km^2, which is mainly affected by the subtropical monsoon climate. It is characterized by the northern mountainous land, which is mainly covered by forest, and the southern plain, which is mainly covered by cultivated land. The annual precipitation in the QR catchment is around 1200 mm, which is concentrated in the mountainous area. The NR catchment is affected by the subtropical monsoon climate and has a drainage area of 41,715 km^2. It is characterized by the forest land. In this catchment, the annual precipitation is from 1200 mm to 1700 mm. When compared to the QR catchment, the average elevation in the NR catchment is low, which may have an effect on the spatial heterogeneity of soil moisture. The YR catchment was chosen to see the spatial heterogeneity of soil moisture in a semi-arid region. It is affected by the continental monsoon climate, with a drainage area of 18,560 km^2. In this catchment, the western mountain area is covered by vegetation, and the eastern plain is covered by loess. When compared to the QR and NR catchments, the YR catchment has less precipitation, with an annual precipitation of less than 700 mm. Since it is hard to simulate soil moisture in catchments that are managed by manmade dams using traditional hydrological models, this study specifically chose the three catchments with an inflow that is almost unaffected by the reservoirs and dams. It is worth noting that the

streamflow data from the Tianyi station in the NR catchment represent the natural inflow runoff to the Tianyi reservoirs and are, thus, not influenced by reservoir regulation.

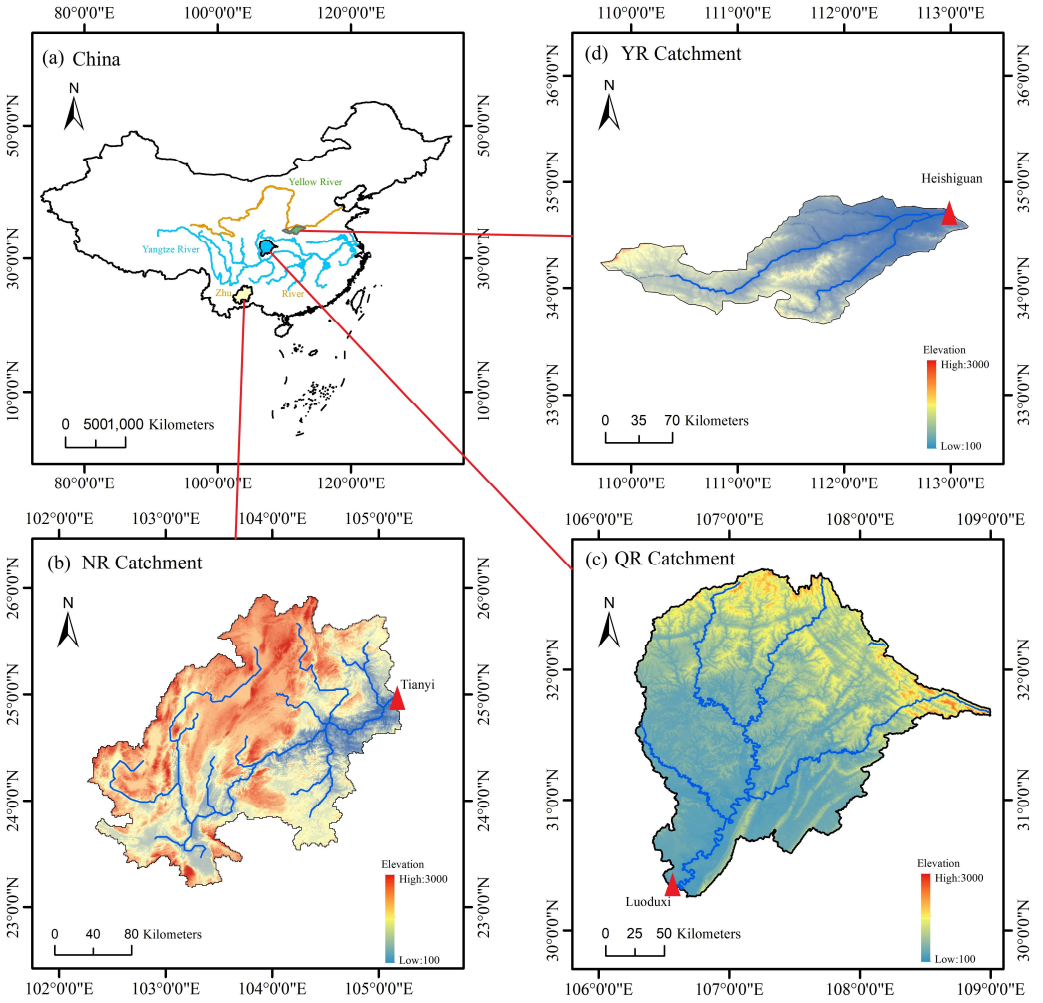

Figure 1. The locations of the chosen catchments in China; details of the (**a**) Nanpan River (NR) catchment, (**b**) Qu River (QR) catchment, (**c**) and Yiluo River (YR) catchment (**d**).

2.2. Remotely Sensed Products

The study chose the European Space Agency Climate Change Initiative (ESA CCI) SM V07.1 COMBINED product (released in May 2022) as the raw satellite product [29–31]. This product combines the measured values of multiple satellite instruments from 1979 to 2021, including Advanced Microwave Instrument-Windscat (AMI-WS), Advanced Scatterometer (ASCAT), Scanning Multichannel Microwave Radiometer (SMMR), Tropical Rainfall Measure Mission Microwave Imager (TMI), Special Sensor Microwave Imager (SSM/I), Advanced Microwave Scanning Radiometer for Earth Observing System (AMSR-E and AMSR2), Microwave Imaging Radiometer using Aperture Synthesis (MIRAS), Soil Moisture Active Passive (SMAP), Global Precipitation Measurement (GPM) Microwave Imager (GMI), Microwave Radiation Imager (MWRI), and WindSat. It provides volumetric soil moisture information (expressed in physical unit m^3/m^3) of the topsoil surface (smaller than 2 cm in terms of thickness) at a spatial scale of approximately 25 km × 25 km. It can be seen that the ESA CCI product has the combined datasets of nearly all the well-known satellite instruments that are related to soil moisture observations. The ESA CCI products have been widely used in hydrological, meteorological, and bio-geochemical systems around the world [32,33]. They have also been validated in China, and results indicate that they have the potential to be further utilized [7].

2.3. Other Data

The meteorological and hydrological data were used for the hydrological model to simulate spatial PSM. The meteorological data include precipitation and potential evapotransporation data, among which the precipitation data were directly acquired from meteorological stations, whereas the potential evapotransporation data were calculated by using the Blaney-Criddle method based on mean temperature data, T_a, and the mean daily percentage of the total annual daytime hours, p, by using the formula $ET_0 = kp(0.46T_a + 8.13)$, where k is the empirical coefficient of crop impact related to sowing time, crop growth, growth period length, and climate, with an initial value of 0.85 in the study [34].

Precipitation and potential evapotransporation data were interpolated by using the inverse distance weighted (IDW) method to match the simulation grids of the hydrological model [35]. The hydrological data refer to the streamflow data acquired from the outlet hydrological stations, including the daily streamflow from the Luoduxi station in the QR catchment, the Tianyi station in the NR catchment, and the Heishiguan station in the YR catchment. These streamflow data were used for the calibration of the hydrological model. By considering the availability of input and calibration data of DDRM in the three chosen catchments, the meteorological and hydrological data from 2013 were used for warming up the model; the data from 2014 to 2016 were used for calibration, and the data from 2017 were used for DDRM modeling to acquire the PSM simulations.

In the study, the driving factors of the spatial heterogeneity of PSM are investigated. Apart from precipitation (PRE), the normalized vegetation index (NDVI), the land use and land cover change (LUCC), the digital elevation model (DEM), soil type (ST), slope (SL), and aspect (AS) were chosen as the potential driving factors. The NDVI data, LUCC data, DEM data, and ST data were acquired from the Resource and Environment Science and Data Center of the Chinese Academy of Sciences "http://www.resdc.cn (accessed on 1 August 2023)". The ST and SL data were calculated based on DEM data through ArcGIS software (version 10.5).

3. Methodology

In order to identify and analyze the differences between the spatial heterogeneity of satellite-based and hydrologically modeled PSM, it is necessary to build datasets that match in terms of their spatial scales and physical characteristics. Since spatial heterogeneity is highly affected by the spatial scales of data, the spatial heterogeneity of the PSM datasets was compared for the satellite spatial scale and modeled spatial scale, respectively. In this section, the methods used to acquire the matched PSM datasets from different sources are first described, followed by the methods used to identify the differences in their spatial heterogeneity and driving factors.

3.1. Acquiring Matched Profile Soil Moisture from a Distributed Hydrological Model

The DEM-based distributed rainfall-runoff model (DDRM) was used in the study to acquire high-resolution (1 km $\times$ 1 km) PSM datasets from the hydrological models. The DDRM is a conceptual distributed rainfall-runoff model developed by Xiong et al. (2004), and it has shown good performance in soil moisture and streamflow simulations in southeast China [36–39].

The model consists of three modules, including grid runoff generation, grid channel runoff routing, and river network runoff routing. In the grid runoff generation module, excess rainfall is generated in the DEM grids under the saturation excess runoff generation mechanism; then, the model routes the excess rainfall in each DEM grid from upstream to downstream for each subcatchment in the grid channel runoff routing module and, furthermore, to the downstream of the whole catchment through the river network in the river network runoff routing module; both are based on the Muskingum method [40]. Details of the model structure and modeling processes of DDRM can be seen in the work of Xiong et al. (2018) and Chen et al. (2022) [36,38]. There are seven saturation excess runoff generation parameters and four routing parameters in the DDRM. Details of these

11 parameters are shown in Table 1. The parameter values used in the study were calibrated by maximizing the objective function of the Nash–Sutcliffe efficiency coefficient (NSE) between the observed and simulated runoff of DDRM in the three chosen catchments using the meteorological and hydrological data from 2014–2016, as per [41].

$$NSE = 1 - \frac{\sum_{t=1}^{T} (Q\mathrm{sim}_t - Qobs_t)^2}{\sum_{t=1}^{T} \left(Qobs_t - \overline{Oobs}\right)^2} \quad (1)$$

$Q\mathrm{sim}_t$ is the simulated runoff at time t, and $Qobs_t$ is the observed runoff at time t. The range of NSE is negative infinity to 1. When NSE approaches 1, it means better model simulation performance. In this study, the spatial scale of DDRM modeling is 1 km × 1 km.

Table 1. Details of DDRM parameters and their calibrated values in the Qu River (QR) catchment, Nanpan River (NR) catchment, and the Yiluo River (YR) catchment. SMC represents soil moisture storage capacity.

Parameter	Description	Range	QR	NR	YR
$S0(mm)$	Minimum SMC throughout the catchment	5–100	88.79	380.33	243.00
$SM(mm)$	Variation range of SMC throughout the catchment	5–700	498.64	480.59	985.61
$a(-)$	Empirical constant reflecting the characteristic of soil water flow	0–1	0.43	0.01	0.01
$b(-)$	Empirical constant reflecting the impact of slope on soil water flow	0–1	0.31	0.71	0.98
$n(-)$	Empirical constant reflecting the degree of heterogeneity of soil water storage capacity	0–1	0.98	0.61	0.85
$TS(h)$	Time constant, reflecting the velocity of the soil water flow	2–200	104.79	345.82	339.80
$TP(h)$	Time constant, reflecting the velocity of the runoff generation	2–200	9.02	160.11	323.27
$c_0(-)$	Grid channel routing parameters with regard to the Muskingum method	0–1	0.99	0.99	0.98
$c_1(-)$	Grid channel routing parameters with regard to the Muskingum method	0–1	0.21	0.01	0.01
$hc_0(-)$	River network routing parameters with regard to the Muskingum method	0–1	0.61	0.80	0.83
$hc_1(-)$	River network routing parameters with regard to the Muskingum method	0–1	0.39	0.10	0.08

DDRM can provide the depth of profile soil moisture ($S_{i,t}$) and its storage capacity (SMC_i) at the grid i and the time step t within 1 km × 1 km by using 1 km × 1 km DEM grids. In order to acquire soil moisture simulations that can match the satellite products, the $S_{i,t}$ from the DDRM is transformed into profile saturation degree (PSD), given in % and calculated as

$$PSD_{i,t}^{Mod} = S_{i,t}/SMC_i \quad (2)$$

where $PSD_{i,t}^{Mod}$ represents DDRM PSD at the modeled grid i and the time step t.

In the study, daily soil moisture datasets within 1 km × 1 km and 25 km × 25 km were built based on the $PSD_{i,t}^{Mod}$ firstly, and then the seasonal averages and annual averages of $PSD_{i,t}^{Mod}$ (from 2017) in each grid were calculated to analyze the spatial heterogeneity during different time periods, among which the datasets within 25 km × 25 km were acquired by resampling $PSD_{i,t}^{Mod}$ within 1 km × 1 km.

3.2. Acquiring Matched Profile Soil Moisture from Remotely Sensed Products

The chosen remotely sensed product provides surface volumetric soil moisture (SVSM), given in m^3m^{-3} for satellite-observed spatial scales. In order to match DDRM PSD, satellite-observed SVSM data were transformed into PSD data in the corresponding spatial scales. When comparing the PSM datasets at a model-simulated spatial scale (1 km × 1 km), the preprocessing procedures of satellite data include the downscale step; when comparing the PSM datasets at a satellite-observed spatial scale, the downscale step is skipped. The framework to acquire matched PSM from the remotely sensed product is shown in Figure 2.

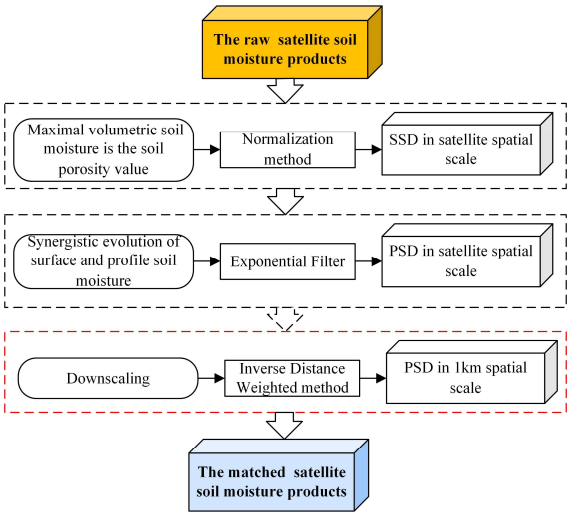

Figure 2. The framework to acquire satellite soil moisture products that match hydrologically modeled soil moisture. The red dashed outline means that this procedure is conducted (or not) according to the needs of comparison scenarios. (SSD: surface saturation degree; PSD: profile saturation degree).

Firstly, the raw satellite soil moisture product was transformed into surface saturation degree (*SSD*) by using the normalization method, which assumes that maximal volumetric soil moisture is the soil porosity value. Since the satellites observe surface soil to acquire land surface information, the remotely sensed products provide only surface soil moisture information, while the DDRM model provides profile soil moisture information. Thus secondly, the *SSD* data were transformed into *PSD* data by using the exponential filter [42]. This filter assumes that the variation in time of deeper soil moisture is linked to the differences between the surface and deeper soil moisture. In this research, the satellite-based PSM is calculated as

$$PSD_{m,t_n}^{Sat} = PSD_{m,t_{n-1}}^{Sat} + K_{t_n}\left[SSD_{m,t_n}^{Sat} - SSD_{m,t_{n-1}}^{Sat}\right] \quad (3)$$

where PSD_{m,t_n}^{Sat} and $PSD_{m,t_{n-1}}^{Sat}$ represent satellite-based *PSD* at the satellite-observed spatial grid m and the observing time point t_n and the previous observing time t_{n-1}, respectively, while SSD_{m,t_n}^{Sat} and $SSD_{m,t_{n-1}}^{Sat}$ represent the corresponding satellite-observed *SSD*. K_{t_n} represents the gain term at the observing time point t_n, and it is calculated as

$$K_{t_n} = K_{t_{n-1}} \Big/ \left[K_{t_{n-1}} + e^{-\left(\frac{t_n - t_{n-1}}{CT}\right)}\right] \quad (4)$$

where $K_{t_1} = 1$ is for the initialization, and CT is the unknown characteristic time length parameter, representing the timescale of the variation in soil moisture to obtain PSM information. The study evaluates the value of CT by maximizing the correlation between satellite-based PSD and hydrologically modeled PSD. Finally, the PSD data at the satellite-observed spatial scale (25 km × 25 km) are downscaled to the hydrologically modeled spatial scale (1 km × 1 km) by using the inverse distance weighted (IDW) method according to the need of the comparison scenarios [35]. In this study, the seasonal averages and annual averages in 2017 for the spatial patterns of satellite-based PSD are also calculated to compare and analyze the spatial heterogeneity during different time periods.

3.3. Identification of Spatial Heterogeneity of Profile Soil Moisture

In each catchment, the spatial heterogeneity of PSM at the 1 km × 1 km and 25 km × 25 km spatial scales from different sources is identified, respectively, by using spatial statistical analysis and the semi-variogram method. In the spatial statistical analysis, the minimum,

maximum, mean, standard deviation, variation, variance, kurtosis, and skewness of the averages of the spatial pattern during different time periods are respectively calculated for the satellite-based and hydrologically modeled PSD. The values of the standard deviation, variation, variance, kurtosis, and skewness represent the spatial variation in the data. In the semi-variogram method, the spatial auto-correlation of the PSM of all datasets is evaluated at first; from this, the spatial correlation of two samples of PSM is quantitatively estimated from their separation distance [43]. Then, the semi-variogram of PSM is calculated as

$$\gamma(h) = \frac{1}{2N}\sum_{i=1}^{N}[z(x_i) - z(x_i + h)]^2 \quad (5)$$

where h represents the distance between samples, N represents the number of samples, and $z(x_i)$ and $z(x_i + h)$ are the PSM values in the spatial positions (x_i) and $(x_i + h)$, respectively. Four theoretical models: linear, spherical, exponential and Gaussian were chosen as the candidate theoretical models to describe the resulting semi-variograms of PSM [27,28]

1. Linear model:

$$\gamma(h) = C_0 + C(h/A) \quad (6)$$

2. Spherical model:

$$\gamma(h) = \begin{cases} 0, (h = 0) \\ C_0 + C\left[1.5(h/A) - 0.5(h/A)^3\right], (0 < h \le A) \\ C_0 + C, (h > A) \end{cases} \quad (7)$$

3. Exponential model:

$$\gamma(h) = \begin{cases} 0, (h = 0) \\ C_0 + C\left[1 - e^{-h/A}\right], (h > 0) \end{cases} \quad (8)$$

4. Gaussian model:

$$\gamma(h) = \begin{cases} 0, (h = 0) \\ C_0 + C\left[1 - e^{-h^2/A^2}\right], (h > 0) \end{cases} \quad (9)$$

where C_0 represents the nugget value, C represents the partial still value, and A is the range. The value of $C/(C + C_0)$ can be used to identify the spatial heterogeneity, which represents weak, medium, and strong spatial heterogeneity at <0.25, 0.25–0.75, and >0.75, respectively.

3.4. Identification of Driving Factors of Spatial Heterogeneity for Profile Soil Moisture

The geographical detector method was used to identify the driving factors of spatial heterogeneity for PSM from different sources. This method can detect the spatial heterogeneity of variables and reveal the driving factors [44,45]. When compared to correlation analysis and linear regression, this method does not assume that there is a nonlinear or linear relationship between different variables, which ensures that the results are not affected by multicollinearity interference between different independent variables. The geographical detector method is composed of factor, ecological, risk, and interaction detectors, among which factor detector is used to calculate the contribution q of variable X to the spatial heterogeneity of the variable Y, which can be expressed as

$$q = 1 - \frac{\sum_{h=1}^{L} N_h \sigma_h^2}{N\sigma^2} \quad (10)$$

where σ_h^2 and σ^2 are the variance in the stratum h and the whole area; N_h and N represent the samples in the stratum h and the total samples. The range of q is 0 to 1. When the value of q is 1, the spatial heterogeneity of Y can be completely explained by X. In the case of this study, PSM is the dependent variable Y, the potential driving factors X include precipitation (PRE), the normalized vegetation index (NDVI), land use and land cover change (LUCC), the digital elevation model (DEM), soil type (ST), slope (SL), and aspect (AS). Since the discrete data of the driving factors are needed in the geographical detector method, the natural breaks in the classification method are used to discretize the PRE, NDVI, DEM, SL, and AS data [46]. The natural breaks classification method, also called the Jenks optimization method, is a data classification method designed to determine the best arrangement of values into different classes. This method is used to reduce the variance within classes and maximize the variance between classes. Thus, when the natural breaks classification method is used to discretize the data, the range of each class is determined by the distribution characteristics of the data and the number of classes they are divided into. In this study, 5 to 15 classes were tested to discretize the data, and nine classes were chosen since the discrete data showed reasonable variances. Moreover, the LUCC and ST data have their own classification system. The LUCC data adopt a two-level classification system: the first level is divided into six classes, mainly based on land resources and their use attributes, including cultivated land, forest land, grassland, water area, construction land, and unused land; the second level is mainly divided into 23 classes based on the natural attributes of land resources. The ST data are digitally generated based on the "1:100,000 Soil Map of the People's Republic of China" compiled and published by the National Soil Census Office in 1995. The traditional "soil occurrence classification" system, which is divided into 12 soil classes covering various types of soil across the country, was adopted.

4. Results

4.1. Spatiotemporal Variations in Satellite-Based and Hydrologically Modeled Profile Soil Moisture

4.1.1. Temporal Variation in Catchment-Averaged Profile Soil Moisture

Temporal variations in the catchment-averaged soil moisture (SSD and PSD) that were acquired based on the ESA CCI product and the DDRM are shown in Figure 3. The corresponding streamflow simulated by the DDRM is also presented in Figure 3. The NSE of the simulated and observed streamflows is 0.74, 0.88, and 0.68 in the QR, NR, and YR catchments, respectively. It can be seen that the DDRM shows better performance for the streamflow simulations in the NR catchment and shows relatively worse performance for the YR catchment. This is because the YR catchment is a semi-arid catchment that is mainly characterized by the infiltration excess runoff generation mechanism, while the DDRM model is built on saturation excess runoff generation. The modeling results are similar to the relevant studies in these three catchments [2,34,35]. Overall, the streamflow simulations have similar change trends to the observed streamflows in all three catchments, which means DDRM has the ability to model the rainfall-runoff processes in the chosen catchments; thus, the intermediate variable simulations, the PSD simulations, can be regarded as containing some useful information.

From the change trends in soil moisture presented in Figure 3, it can be seen that the changing amplitude of ESA CCI SSD is larger than that of ESA CCI PSD. This is because the surface soil moisture varies with the rapid meteorological changes, but the change in the amplitude of soil moisture would be largely weakened by the redistribution of soil layers when water is transported from surface to profile. Moreover, DDRM PSD shows a larger changing amplitude than ESA CCI SSD and PSD, which is mainly manifested in obviously smaller minimum values for DDRM PSD. This may due to the fact that DDRM PSD is less reliable in the low values for two reasons. Firstly, the model is built based on saturation excess runoff generation, which means that there is no limitation of soil moisture simulations before the soil is saturated. Secondly, the objective function used to calibrate the DDRM model parameters in the study, the NSE of the simulated and observed streamflows, generally shows worse performance in fitting low values. Moreover, since

there are uncertainties in both ESA CCI and DDRM PSD, it is hard to say which one is more reliable. Overall, the ESA CCI PSD and DDRM PSD data show similar temporal tendencies over seasonal changes, which means the PSD data acquired from ESA CCI and DDRM can be reliable for time; this further indicates that these PSD data have potential to provide some useful spatial information.

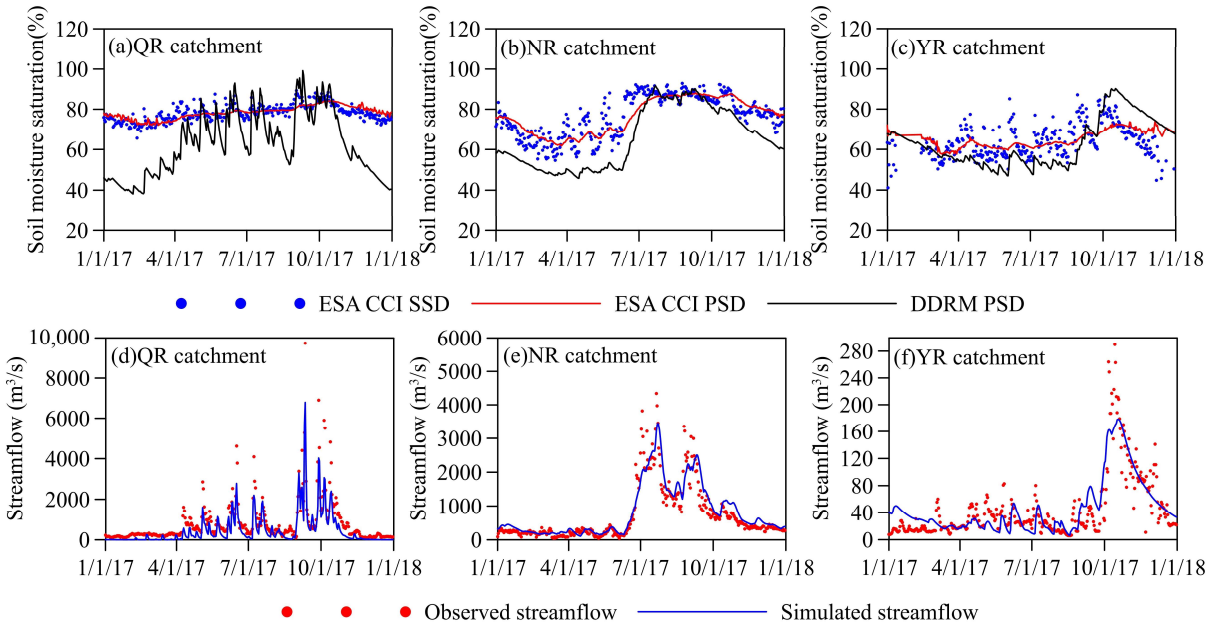

Figure 3. Time series of catchment-averaged surface saturation degree (SSD) and profile saturation degree (PSD) acquired from ESA CCI, and PSD simulated by DDRM (**a**–**c**), with the corresponding streamflow simulated by DDRM (**d**–**f**) in the QR, NR, and YR catchments.

4.1.2. Spatial Variation in Profile Soil Moisture

The spatial patterns in the ESA CCI and DDRM PSD averages for different seasons and the whole year of 2017 are shown in Figures 4–6 for the QR catchment, NR catchment, and YR catchment, respectively. In the 1 km × 1 km spatial scales, the sample sizes of the PSD datasets are 39,211, 41,715, and 18,560 in the QR, NR, and YR catchments, respectively, and in the 25 km × 25 km spatial scales, the sample sizes are 63, 67, and 30 for the three catchments. From the figures, it can be seen that there is an obviously gradual trend in DDRM PSD from the upstream area to the downstream area, while ESA CCI PSD has no similar trend. This is because the simulation processes of DDRM PSD in each grid of the model are affected by the PSD values of other grids, but the observation and retrieval process of ESA CCI PSD in each grid is relatively independent. Moreover, it can be seen that both the ESA CCI PSD and the DDRM PSD data show higher values in the low-elevation areas (normally downstream) than in the high-elevation areas (normally upstream). This means that the elevation or slope may be the key driving factors of PSD. Moreover, the river network in each catchment is clearly displayed in the spatial distribution map of the DDRM PSD averages. This is due to the saturation excess runoff generation mechanism applied in DDRM, where the soil is always saturated in the grid points of the river network, which means PSD always equals 1 in the grids of the river network.

When comparing the spatial patterns of PSD in different seasons (January–March, April–June, July–September, October–December, shown as Jan–Mar, Apr–Jun, Jul–Sept, Oct–Dec respectively), it can be seen that the spatial patterns of ESA CCI and DDRM PSD show similar changing trends from January to December. In the QR catchment and NR catchment, the values of PSD spatial data are relatively high in the Jul–Sept period, and in the YR catchment, those are higher in the Oct–Dec period, which is consistent with the changing trends in the corresponding time series, as shown in Figure 3. This is because the

rainfall values are concentrated in the Jul–Sept period for the QR and NR catchments and in the Oct–Dec period for the YR catchment. When comparing the spatial patterns of PSD in catchments with different climate conditions, the spatial distribution of ESA CCI PSD is similar to the DDRM PSD in the QR and the NR catchments, while that of ESA CCI PSD is different from that of DDRM PSD in the YR catchment, where the DDRM PSD patterns show higher values in the downstream but the ESA CCI PSD patterns show higher values in the upstream. The reason is that the runoff generation mechanism used in DDRM is different from the actual mechanism in the YR catchment. Moreover, the loess covering the eastern plain in the YR catchment also affects the actual spatial distribution of PSD patterns. On the whole, the spatial variations in ESA CCI and DDRM PSD are, overall, consistent and locally different; the possible driving factors of the PSD spatial patterns can be studied further.

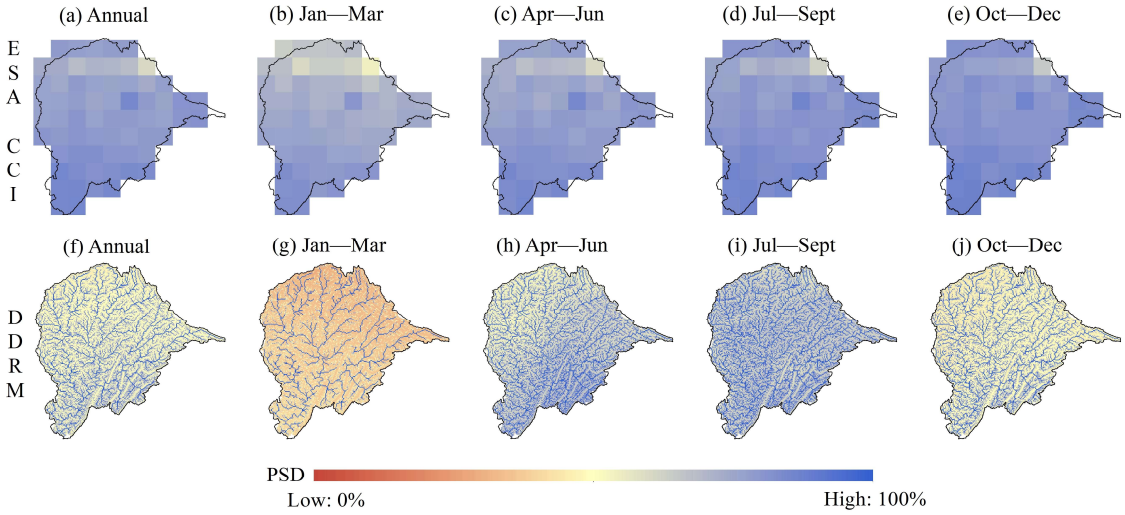

Figure 4. The spatial pattern of the annual averages and every-four-months averages of profile saturation degree (PSD) acquired from ESA CCI ((**a**–**e**), 25 km × 25 km) and DDRM ((**f**–**j**), 1 km × 1 km) in the QR catchment during 2017.

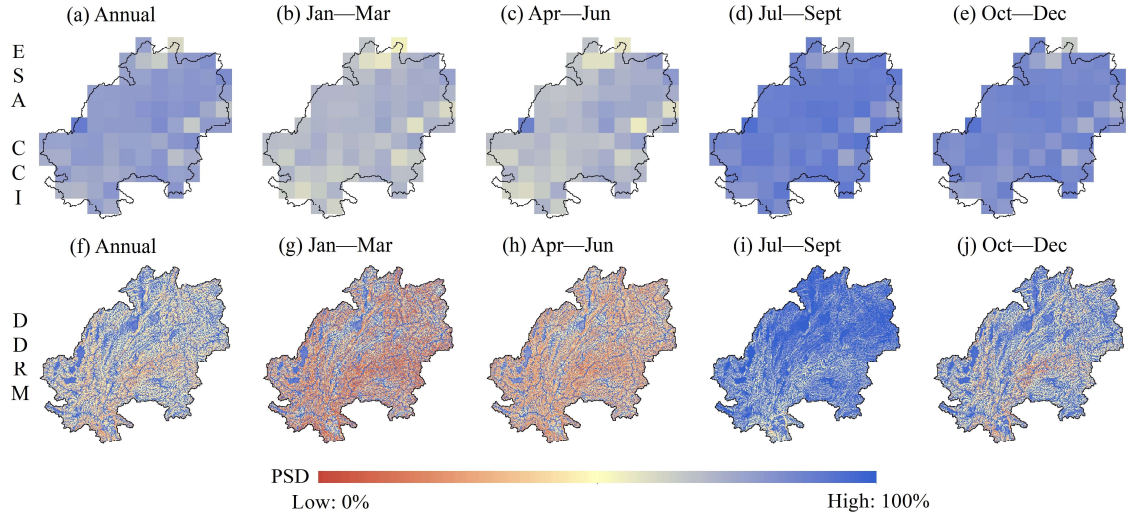

Figure 5. The spatial pattern of the annual averages and seasonal averages of profile saturation degree (PSD) acquired from ESA CCI ((**a**–**e**), 25 km × 25 km) and DDRM ((**f**–**j**), 1 km × 1 km) in the NR catchment during 2017.

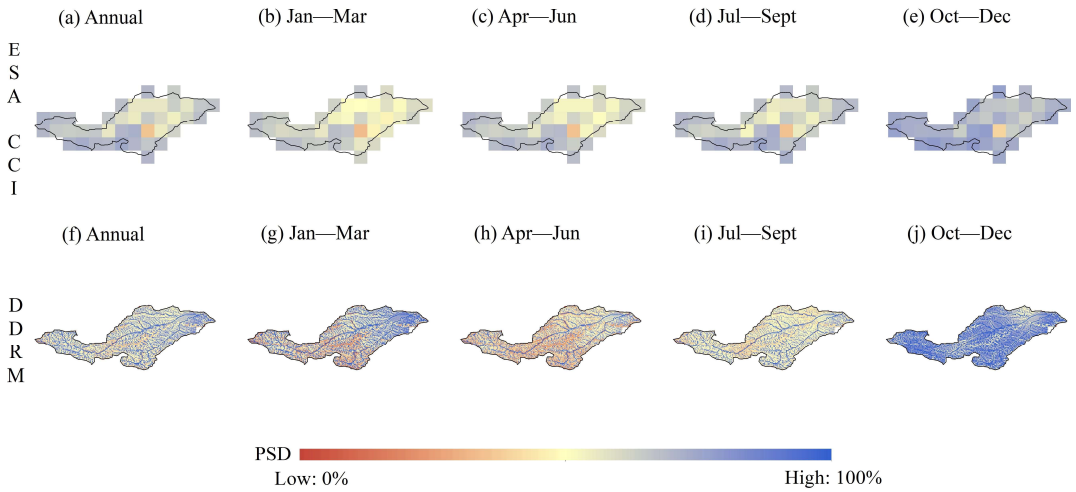

Figure 6. The spatial pattern of the annual averages and seasonal averages of profile saturation degree (PSD) acquired from ESA CCI ((**a**–**e**), 25 km × 25 km) and DDRM ((**f**–**j**), 1 km × 1 km) in the YR catchment during 2017.

4.2. The Identification of the Spatial Heterogeneity of Satellite-Based and Hydrologically Modeled Profile Soil Moisture

4.2.1. Spatial Statistical Analysis of Satellite-Based and Hydrologically Modeled Profile Soil Moisture

The boxplots (extremum, standard deviation, mean) of the spatial data of the ESA CCI and DDRM PSD temporal averages for multiple periods are shown in Figures 7–9 for the QR, NR, and YR catchments, and the descriptive statistics of the spatial data are presented in the Tables 2–4. It can be seen that the spatial scale is one of the driving factors of the spatial heterogeneity of profile soil moisture. When the ESA CCI PSD within a 25 km × 25 km spatial scale grid is downscaled to the grid of 1 km × 1 km scale, most of the spatial statistical values decrease for all three catchments; for example, the variation in the spatial pattern of the PSD averages for the whole year in the QR catchment reduces from 5.55% to 3.87%; in the NR catchment, this reduces from 5.96% to 3.30%; in the YR catchment, this reduces from 11.23% to 6.49%. When the DDRM PSD within a 1 km × 1 km spatial scale grid is upscaled to the grid of 25 km × 25 km scale, the change in the spatial statistical values is also significant. For all catchments, the ranges of the DDRM PSD values within 1 km × 1 km scale are nearly twice those of the values at the 25 km × 25 km scale. It can be seen that most of the spatial statistical values decrease after spatial rescaling for all catchments in this study, whether it is upscaling or downscaling. This is because there is no new information added to the spatial distribution of PSD in the spatial upscaling method (resampling method) and the spatial downscaling method (IDW method) used in this study, but partial information may be lost or changed during the spatial rescaling.

When comparing the spatial statistical values of ESA CCI and DDRM PSD at the same spatial scale, the values for range, standard deviation, and some of the other statistical values of DDRM PSD are higher than ESA CCI PSD in nearly all the cases. The different spatial scales of the raw data of ESA CCI and DDRM PSD may be one of the reasons for this; it indicates that DDRM PSD shows higher spatial heterogeneity than the ESA CCI PSD for the same spatial scale. When comparing the spatial statistical values of PSD in the different seasons of 2017, the standard deviation, variation, and such spatial statistics are higher during the low-flow period of each catchment, which reveals the spatial heterogeneity to some extent; for instance, the period of Jan–Mar shows the highest standard deviations for DDRM PSD at the 1 km × 1 km spatial scale, which are 18.98, 32.19, and 26.01 for the QR, NR, and YR catchments, respectively. This is because the soil in most of the grids in the catchments tends to be saturated in the high-flow period, in which case PSD approaches 1, and the spatial heterogeneity of PSD decreases. When comparing the spatial statistical

values of the PSD spatial patterns with different climate conditions in catchments, the changing trends of the PSD values over the seasons are in accordance with the runoff changes in all catchments. In the QR and NR catchments, the period of Jul–Sept shows higher PSD values, and in the YR catchment, the PSD values for the Oct–Dec period are higher. This is because the climate conditions in the YR catchment are different from the other two catchments, and the rainfall concentration period is later than that of the QR and NR catchments.

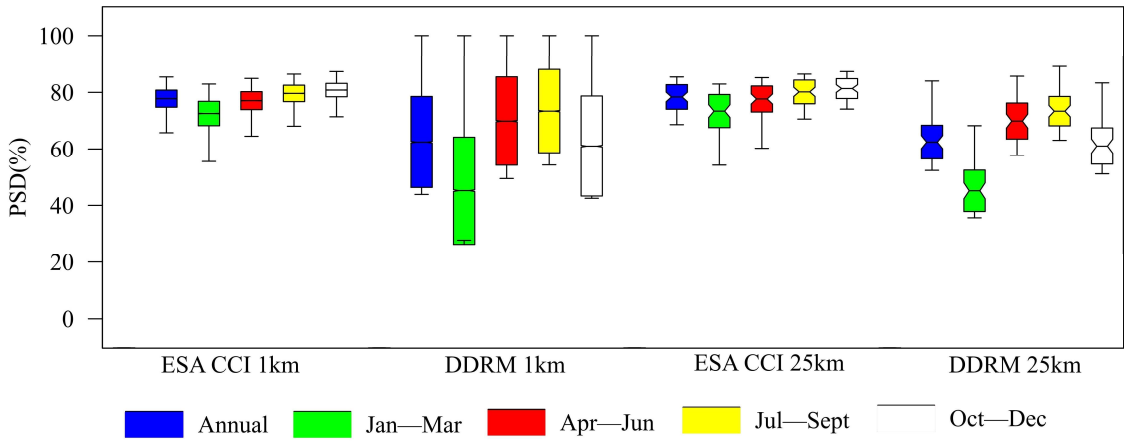

Figure 7. The boxplots (extremum, standard deviation, and mean) of the spatial data of ESA CCI and DDRM profile saturation degree (PSD) temporal averages in the QR catchment.

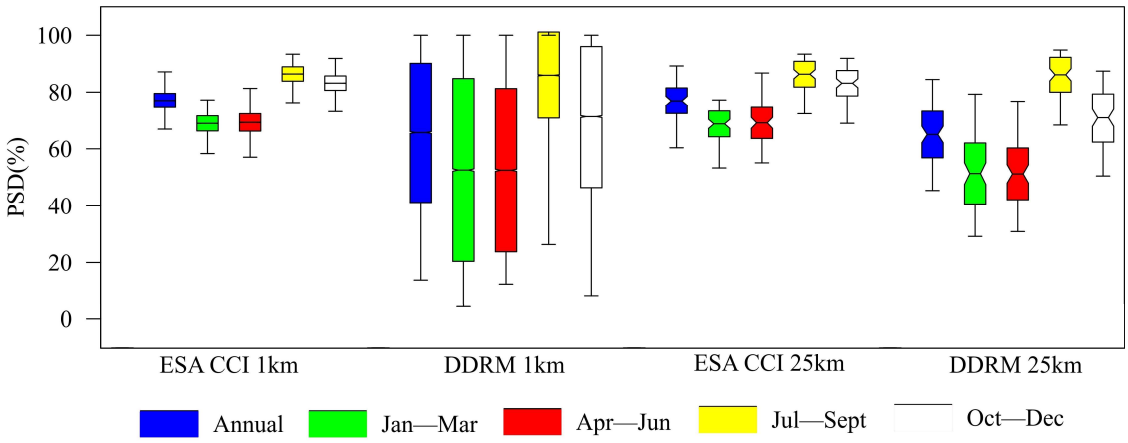

Figure 8. The boxplots (extremum, standard deviation, and mean) of the spatial data of satellite-based and hydrologically modeled profile saturation degree (PSD) temporal averages in the NR catchment.

Table 2. Descriptive statistics of the spatial data of ESA CCI and DDRM profile saturation degree (PSD) temporal averages in the QR catchment.

	Minimum	Maximum	Mean	Standard Deviation	Variation	Variance	Kurtosis	Skewness
				ESA CCI PSD in 1 km × 1 km				
Annual	60.82	85.44	77.78	3.01	3.87	0.09	1.91	−0.65
Jan–Mar	54.25	82.93	72.55	4.30	5.92	0.18	0.00	−0.28
Apr–Jun	60.26	84.94	77.08	3.16	4.11	0.10	1.23	−0.51
Jul–Sept	62.53	86.44	79.64	2.89	3.63	0.08	2.33	−0.91
Oct–Dec	64.93	87.35	80.81	2.36	2.92	0.06	4.75	−0.95

Table 2. *Cont.*

	Minimum	Maximum	Mean	Standard Deviation	Variation	Variance	Kurtosis	Skewness
DDRM PSD in 1 km × 1 km								
Annual	43.86	100.00	62.44	16.11	25.80	2.59	0.26	1.23
Jan–Mar	27.70	100.00	45.21	18.98	41.99	3.60	3.36	2.15
Apr–Jun	49.48	100.00	69.86	15.62	22.36	2.44	−0.79	0.80
Jul–Sept	54.30	100.00	73.39	14.74	20.08	2.17	−0.96	0.80
Oct–Dec	42.50	100.00	61.02	17.71	29.02	3.14	−0.02	1.17
ESA CCI PSD in 25 km × 25 km								
Annual	60.82	85.45	78.39	4.35	5.55	0.19	3.27	−1.19
Jan–Mar	54.24	82.95	73.40	5.84	7.96	0.34	0.81	−0.72
Apr–Jun	60.25	85.19	77.67	4.59	5.91	0.21	2.24	−0.98
Jul–Sept	62.53	86.45	80.17	4.19	5.22	0.18	4.06	−1.47
Oct–Dec	64.92	87.36	81.35	3.51	4.31	0.12	6.38	−1.48
DDRM PSD in 25 km × 25 km								
Annual	52.37	84.02	62.44	5.95	9.54	0.35	2.11	1.17
Jan–Mar	35.62	77.72	45.16	7.31	16.19	0.53	6.38	2.17
Apr–Jun	57.73	85.71	69.88	6.36	9.10	0.40	−0.32	0.30
Jul–Sept	63.07	89.21	73.38	5.18	7.06	0.27	0.67	0.79
Oct–Dec	51.15	83.34	61.05	6.42	10.52	0.41	1.56	1.14

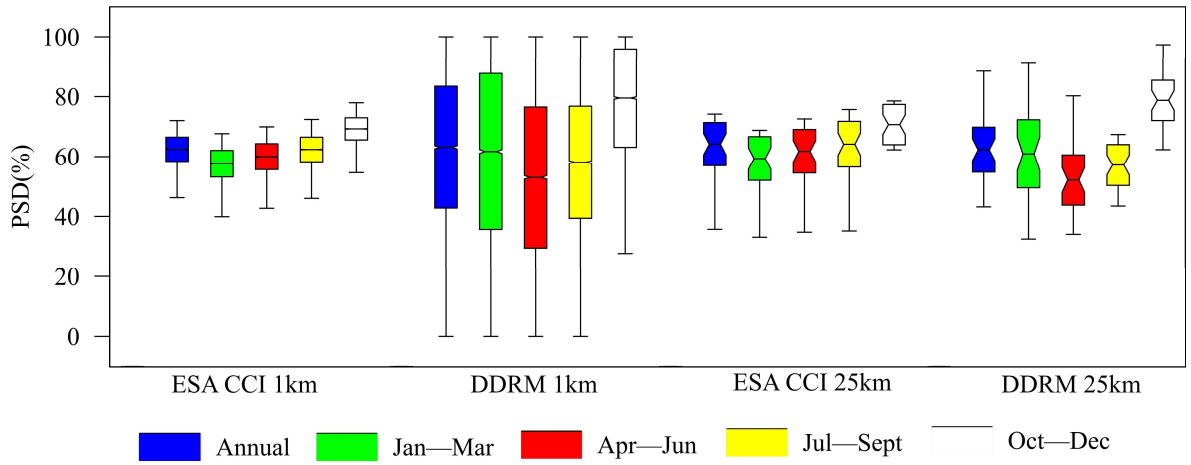

Figure 9. The boxplots (extremum, standard deviation, and mean) of the spatial data of satellite-based and hydrologically modeled profile saturation degree (PSD) temporal averages in the YR catchment.

4.2.2. The Semi-Variogram Analysis of Satellite-Based and Hydrologically Modeled Profile Soil Moisture

The optimal theoretical semi-variogram models and the related parameters for the spatial data of DDRM and ESA CCI PSD temporal averages during different periods of 2017 in the three catchments are presented in Tables 5–7. At the 1 km × 1 km spatial scale, the optimal theoretical semi-variogram model for the ESA CCI PSD is determined to be the Gaussian model, and for DDRM PSD, it is confirmed to be the exponential model in all three catchments. At the 25 km × 25 km spatial scale, the optimal theoretical semi-variogram model for ESA CCI PSD is the Gaussian model for the QR and YR catchments, and the exponential model is optimal for the NR catchment. Overall, the Gaussian model and the exponential model are the common optimal semi-variogram models for PSD spatial data in the study.

Table 3. Descriptive statistics of the spatial data of satellite-based and hydrologically modeled profile saturation degree (PSD) temporal averages in the NR catchment.

	Minimum	Maximum	Mean	Standard Deviation	Variation	Variance	Kurtosis	Skewness
				ESA CCI PSD in 1 km × 1 km				
Annual	60.37	89.18	77.02	2.54	3.30	0.06	5.57	−1.56
Jan–Mar	53.33	77.22	68.88	2.64	3.83	0.07	3.27	−1.20
Apr–Jun	55.12	86.68	69.22	3.04	4.39	0.09	1.76	−0.12
Jul–Sept	67.18	93.36	86.39	2.53	2.93	0.06	9.31	−2.47
Oct–Dec	64.20	91.88	83.17	2.54	3.05	0.06	8.62	−2.29
				DDRM PSD in 1 km × 1 km				
Annual	13.77	100.00	65.68	24.47	37.25	5.99	−1.40	0.08
Jan–Mar	4.30	100.00	52.59	32.19	61.21	10.36	−1.46	0.31
Apr–Jun	12.33	100.00	52.51	28.75	54.75	8.27	−1.25	0.55
Jul–Sept	26.32	100.00	85.94	15.19	17.67	2.31	−0.37	−0.85
Oct–Dec	8.28	100.00	71.23	24.80	34.81	6.15	−1.27	−0.30
				ESA CCI PSD in 25 km × 25 km				
Annual	60.36	89.22	76.91	4.58	5.96	0.21	2.76	−1.17
Jan–Mar	53.32	77.22	68.70	4.50	6.55	0.20	1.56	−1.10
Apr–Jun	55.09	86.74	69.05	5.45	7.89	0.30	1.04	−0.02
Jul–Sept	67.17	93.38	86.33	4.53	5.24	0.20	4.85	−1.99
Oct–Dec	64.18	91.91	83.14	4.47	5.38	0.20	4.81	−1.91
				DDRM PSD in 25 km × 25 km				
Annual	45.42	84.45	65.00	8.14	12.52	0.66	−0.28	−0.01
Jan–Mar	29.19	79.28	51.35	10.67	20.79	1.14	−0.10	0.24
Apr–Jun	30.89	76.76	51.23	9.06	17.68	0.82	0.36	0.56
Jul–Sept	68.29	94.82	86.12	6.13	7.11	0.38	0.28	−0.87
Oct–Dec	50.50	87.40	70.84	8.51	12.01	0.72	−0.55	−0.26

Table 4. Descriptive statistics of the spatial data of satellite-based and hydrologically modeled profile saturation degree (PSD) temporal averages in the YR catchment.

	Minimum	Maximum	Mean	Standard Deviation	Variation	Variance	Kurtosis	Skewness
				ESA CCI PSD in 1 km × 1 km				
Annual	35.81	72.02	62.44	4.05	6.49	0.16	4.25	−1.11
Jan–Mar	33.18	67.65	57.61	4.46	7.74	0.20	1.53	−0.63
Apr–Jun	34.86	69.93	59.97	4.34	7.24	0.19	1.96	−0.60
Jul–Sept	35.26	72.41	62.38	4.12	6.60	0.17	4.35	−1.16
Oct–Dec	39.74	77.95	69.26	3.69	5.33	0.14	11.41	−2.24
				DDRM PSD in 1 km × 1 km				
Annual	0.00	100.00	63.11	20.33	32.21	4.13	−0.45	0.20
Jan–Mar	0.00	100.00	61.71	26.01	42.16	6.77	−1.11	0.00
Apr–Jun	0.00	100.00	53.00	23.52	44.39	5.53	−0.68	0.56
Jul–Sept	0.00	100.00	58.09	18.71	32.21	3.50	0.33	0.70
Oct–Dec	0.00	100.00	79.52	16.41	20.63	2.69	2.65	−0.96
				ESA CCI PSD in 25 km × 25 km				
Annual	35.74	74.18	64.14	7.20	11.23	0.52	4.61	−1.65
Jan–Mar	33.11	68.77	59.34	7.32	12.33	0.54	2.67	−1.33
Apr–Jun	34.78	72.57	61.77	7.28	11.78	0.53	3.23	−1.37
Jul–Sept	35.18	75.71	64.13	7.64	11.91	0.58	3.72	−1.49
Oct–Dec	39.65	78.53	70.68	6.70	9.48	0.45	10.60	−2.57
				DDRM PSD in 25 km × 25 km				
Annual	43.16	88.51	62.28	7.52	12.08	0.57	3.14	0.71
Jan–Mar	32.49	91.14	60.91	11.38	18.68	1.30	0.63	0.23
Apr–Jun	34.06	80.25	52.15	8.41	16.12	0.71	2.20	0.76
Jul–Sept	43.44	85.29	57.17	6.86	11.99	0.47	6.19	1.58
Oct–Dec	62.32	97.34	78.74	6.71	8.52	0.45	0.89	−0.07

Table 5. Optimal theoretical semi-variogram models and their related parameters for the spatial data of ESA CCI and DDRM profile saturation degree (PSD) temporal averages in the QR catchment.

	Theoretical Model	Nugget	Still	Proportion $C/(C_0 + C)$	Range (m)	Coefficient of Determination	Residual Sum of Squares ($\%^2$)
			ESA CCI PSD in 1 km × 1 km				
Annual	Gaussian	0.00001	0.00324	0.997	10,456	0.808	0.3127
Jan–Mar	Gaussian	0.000001	0.00250	0.999	10,549	0.814	0.1723
Apr–Jun	Gaussian	0.00001	0.00356	0.997	10,806	0.825	0.3706
Jul–Sept	Gaussian	0.00001	0.00347	0.997	10,447	0.808	0.3614
Oct–Dec	Gaussian	0.000001	0.00290	0.999	10,468	0.809	0.2423
			DDRM PSD in 1 km × 1 km				
Annual	Exponential	0.0042	0.0522	0.920	1830	0.972	0.028
Jan–Mar	Exponential	0.0077	0.0984	0.922	2220	0.947	0.337
Apr–Jun	Exponential	0.0003	0.0402	0.993	1500	0.956	0.015
Jul–Sept	Exponential	0.0033	0.0354	0.907	1590	0.970	0.008
Oct–Dec	Exponential	0.0056	0.0660	0.915	1860	0.975	0.041
			ESA CCI PSD in 25 km × 25 km				
Annual	Gaussian	0.0117	0.0703	0.834	86,009	0.656	70.33
Jan–Mar	Gaussian	0.008	0.0912	0.912	85,437	0.697	130
Apr–Jun	Gaussian	0.0122	0.081	0.849	84,364	0.634	100
Jul–Sept	Gaussian	0.0125	0.0654	0.809	88,400	0.681	52.88
Oct–Dec	Gaussian	0.01069	0.03718	0.712	85,804	0.710	9.933
			DDRM PSD in 25 km × 25 km				
Annual	Spherical	0.00001	0.00788	0.999	38,300	0.505	0.0013
Jan–Mar	Exponential	0.0002	0.0199	0.990	48,900	0.688	0.02563
Apr–Jun	Spherical	0.00014	0.00696	0.980	86,207	0.514	0.0615
Jul–Sept	Exponential	0.0002	0.00476	0.958	28,500	0.884	0.0003
Oct–Dec	Spherical	0.00001	0.00969	0.999	37,400	0.568	0.0010

The proportion of $C/(C_0 + C)$ in the semi-variogram model can represent the spatial heterogeneity of the data. For all cases, the proportion of $C/(C_0 + C)$ is higher than 0.75, which means that the spatial data of both ESA CCI and DDRM PSD show strong spatial heterogeneity in different seasons, different spatial scales, and different catchments. It should be noted that scale dependency is one of the most important characteristics of the spatial heterogeneity of the data. For the data in different spatial ranges, it is hard to distinguish which spatial data have stronger spatial heterogeneity. In the study, one of the parameters in the optimal theoretical semi-variogram models—the range—shows a significant difference for the different spatial data of ESA CCI PSD and DDRM PSD. The range parameter is around 10,000 m for ESA CCI PSD at 1 km × 1 km for all three catchments, and it is around 1500 m for DDRM PSD at 1 km × 1 km. In contrast, the range parameter is much higher for ESA CCI PSD and DDRM PSD at 25 km × 25 km. For the optimal theoretical semi-variogram models, it can be seen that this parameter is dissimilar when the spatial data are in the same spatial scale. This is because the data of ESA CCI PSD at 1 km × 1 km and DDRM PSD at 25 km × 25 km are not the raw data. Thus, it is hard to compare the spatial heterogeneity of these data through the $C/(C_0 + C)$ proportion. Since the range parameter is similar in the different seasons of each of the spatial datasets, it can be seen that spatial data in the low-flow period mostly show larger spatial heterogeneity than those in the high-flow period. In addition, since the range parameter in different catchments is also similar when comparing data from one source, it can be found that the PSD data in the YR catchment show higher spatial heterogeneity, and those in the QR catchment show relatively low spatial heterogeneity, meaning that the spatial heterogeneity of profile soil moisture is higher in a semi-arid catchment.

Table 6. Optimal theoretical semi-variogram models and their related parameters for the spatial data of ESA CCI and DDRM profile saturation degree (PSD) temporal averages in the NR catchment.

	Theoretical Model	Nugget	Still	Proportion $C/(C_0 + C)$	Range (m)	Coefficient of Determination	Residual Sum of Squares ($\%^2$)
			ESA CCI PSD in 1 km × 1 km				
Annual	Gaussian	0.00001	0.00348	0.997	10,504	0.835	0.2898
Jan–Mar	Gaussian	0.00001	0.00475	0.998	10,402	0.831	0.5596
Apr–Jun	Gaussian	0.00001	0.00373	0.997	10,697	0.844	0.3201
Jul–Sept	Gaussian	0.00001	0.00432	0.998	10,350	0.826	0.4711
Oct–Dec	Gaussian	0.00001	0.00363	0.997	10,843	0.847	0.3045
			DDRM PSD in 1 km × 1 km				
Annual	Exponential	0.0047	0.0761	0.938	1620	0.819	0.3403
Jan–Mar	Exponential	0.3100	5.0100	0.938	1680	0.820	1650
Apr–Jun	Exponential	0.0209	0.2968	0.930	1710	0.823	6.075
Jul–Sept	Exponential	0.0001	0.0363	0.997	1440	0.702	0.1082
Oct–Dec	Exponential	0.0035	0.0683	0.949	1560	0.766	0.3376
			ESA CCI PSD in 25 km × 25 km				
Annual	Exponential	0.0012	0.0682	0.982	63,900	0.752	0.5022
Jan–Mar	Exponential	0.001	0.0346	0.971	74,400	0.801	0.1357
Apr–Jun	Exponential	0.00028	0.02826	0.990	68,100	0.803	0.0813
Jul–Sept	Exponential	0.00005	0.0281	0.998	60,000	0.721	0.08278
Oct–Dec	Exponential	0.00057	0.02484	0.977	72,300	0.815	0.0576
			DDRM PSD in 25 km × 25 km				
Annual	Spherical	0.0001	0.0412	0.998	41,500	0.334	0.1401
Jan–Mar	Exponential	0.016	0.54	0.970	42,000	0.420	26.76
Apr–Jun	Spherical	0.0001	0.0369	0.997	31,800	0.511	0.06259
Jul–Sept	Exponential	0.0244	0.0737	0.669	38,156	0.569	47.5
Oct–Dec	Exponential	0.0023	0.0522	0.956	49,500	0.639	0.215

4.3. Contribution of Driving Factors to the Spatial Heterogeneity of Profile Soil Moisture

Tables 8–10 show the *q* statistics of the different driving factors of the spatial distribution of ESA CCI PSD and DDRM PSD, respectively, at 1 km × 1 km using the geographical detector method. It can be found that although the *q* values of the different driving factors of the spatial heterogeneity of ESA CCI PSD and DDRM PSD are quite different but the orders of relative importance are similar. In the QR and YR catchments, DEM contributes most to the spatial heterogeneity of both ESA CCI PSD and DDRM PSD, for which the QR catchment average *q* value is 0.308 for ESA CCI PSD and 0.121 for DDRM PSD, and in the YR catchment, it was 0.291 for ESA CCI PSD and 0.089 for DDRM PSD. PRE is the second-most important driving factor for both ESA CCI PSD and DDRM PSD in these two catchments, in which the average *q* value is 0.266 for ESA CCI PSD and 0.029 for DDRM PSD in the QR catchment and 0.159 for ESA CCI PSD, 0.033 for DDRM PSD in the YR catchment. The importance of PRE in terms of the spatial heterogeneity of PSD in this study is consistent with a previous paper, which found that PRE contributes more than 60% of the spatial heterogeneity of GLDAS-2.1 (Global Land Data Assimilation System-2.1) SM products [22]. Further, ST is the third-most important driving factor in the QR and YR catchment. It can also be noticed that the NR catchment shows different orders of relative importance in terms of driving factors. For the ESA CCI PSD, the importance is PRE > ST > DEM, and for the DDRM PSD, the order is LUCC > ST > NDVI. This may be due to the fact that the amount of classes of ST in the NR catchment is greater than those in the QR and YR catchments, which is above 30 in the NR catchment and is around 20 in the QR and YR catchments. Moreover, slope and aspect show little influence on the spatial heterogeneity of both ESA CCI PSD and DDRM PSD in all three catchments; this may be due to the slope aspect being more likely to influence water flow in the surface soil by gravity and evapotranspiration, but it shows little direct influence on deeper soil moisture.

Table 7. Optimal theoretical semi-variogram models and their related parameters for the spatial data of ESA CCI and DDRM profile saturation degree (PSD) temporal averages in the YR catchment.

	Theoretical Model	Nugget	Still	Proportion $C/(C_0 + C)$	Range (m)	Coefficient of Determination	Residual Sum of Squares ($\%^2$)
			ESA CCI PSD in 1 km × 1 km				
Annual	Gaussian	0.00001	0.0095	0.999	10,458	0.813	2.758
Jan–Mar	Gaussian	0.00001	0.00937	0.999	10,845	0.833	2.505
Apr–Jun	Gaussian	0.00001	0.00942	0.999	10,861	0.831	2.608
Jul–Sept	Gaussian	0.00001	0.01012	0.999	10,810	0.832	2.919
Oct–Dec	Gaussian	0.00001	0.00847	0.999	10,977	0.835	2.052
			DDRM PSD in 1 km × 1 km				
Annual	Exponential	0.0017	0.0385	0.956	1680	0.918	0.03359
Jan–Mar	Exponential	0.0001	0.0592	0.998	1350	0.648	0.1828
Apr–Jun	Exponential	0.013	2.474	0.995	1830	0.908	229
Jul–Sept	Exponential	0.00159	0.03288	0.952	1770	0.952	0.01684
Oct–Dec	Exponential	0.00001	0.02222	0.999	2040	0.948	0.01581
			ESA CCI PSD in 25 km × 25 km				
Annual	Gaussian	0.0001	0.0368	0.997	52,654	0.642	4.481
Jan–Mar	Gaussian	0.0001	0.0425	0.998	58,196	0.727	4.333
Apr–Jun	Gaussian	0.0001	0.0381	0.997	56,811	0.719	3.572
Jul–Sept	Gaussian	0.0001	0.0383	0.997	52,307	0.627	5.211
Oct–Dec	Gaussian	0.00001	0.0309	0.999	48,670	0.539	4.400
			DDRM PSD in 25 km × 25 km				
Annual	Gaussian	0.00001	0.01452	0.999	50,575	0.652	0.4635
Jan–Mar	Exponential	0.001	0.756	0.999	62,790	0.822	4810
Apr–Jun	Gaussian	0.00001	0.02652	0.999	52,654	0.703	1.254
Jul–Sept	Gaussian	0.00001	0.01322	0.999	46,765	0.679	0.2381
Oct–Dec	Gaussian	0.0001	0.0366	0.997	56,118	0.704	2.960

Table 8. The q statistics of different driving factors on the spatial distribution of ESA CCI and the DDRM profile saturation degree (PSD) temporal averages of the QR catchment in the geographical detector method.

	PRE	NDVI	LUCC	DEM	ST	SL	AS
			ESA CCI PSD in 1 km × 1 km				
Annual	0.0413	0.1487	0.0879	0.2959	0.1439	0.0814	0.0082
Jan–Mar	0.6889	0.0248	0.1510	0.4453	0.2296	0.1002	0.0096
Apr–Jun	0.2848	0.1849	0.0852	0.2924	0.1394	0.0803	0.0095
Jul–Sept	0.2074	0.1391	0.0747	0.2584	0.1428	0.0697	0.0081
Oct–Dec	0.1098	0.0824	0.0711	0.2492	0.1435	0.0767	0.0062
Averaged	0.2664	0.1160	0.0940	0.3082	0.1598	0.0817	0.0083
			DDRM PSD in 1 km × 1 km				
Annual	0.0099	0.0272	0.0165	0.1245	0.0227	0.0137	0.0004
Jan–Mar	0.0184	0.0048	0.0172	0.1182	0.0309	0.0170	0.0005
Apr–Jun	0.1009	0.0173	0.0144	0.1402	0.0288	0.0123	0.0019
Jul–Sept	0.0038	0.0291	0.0168	0.1027	0.0194	0.0067	0.0005
Oct–Dec	0.0108	0.0217	0.0180	0.1190	0.0196	0.0178	0.0004
Averaged	0.0287	0.0200	0.0166	0.1209	0.0243	0.0135	0.0007

When comparing the contribution of driving factors to the spatial heterogeneity of profile soil moisture in different seasons, it can be found that the influence of PRE on PSD varies greatly with seasons. PRE contributes little to the spatial heterogeneity of annual PSD averages; this is because annual averages smooth out the difference in changes within the year. For ESA CCI PSD, PRE contributes most to the Jan–Mar period, the contribution is 68.89% (q = 0.6889), 23.61% (q = 0.2361), and 36.22% (q = 0.3622), respectively, in the three catchments. It may be because when most of the soil is unsaturated in the low-flow period, the soil moisture responds quickly to PRE. For DDRM PSD, PRE contributes most to the

Apr–Jun period, Jul–Sept period, and Oct–Dec period, respectively, in the three catchments. This may be because the soil moisture calculation module of DDRM is controlled not only by PRE but also by antecedent rainfall, soil moisture storage capacity, flowing mechanism, etc., and there is model structure uncertainty during the soil moisture simulations.

Table 9. The q statistics of the different driving factors on the spatial distribution of ESA CCI and the DDRM profile saturation degree (PSD) temporal averages of the NR catchment in the geographical detector method.

	PRE	NDVI	LUCC	DEM	ST	SL	AS
			ESA CCI PSD in 1 km × 1 km				
Annual	0.0368	0.0128	0.0236	0.0545	0.0856	0.0003	0.0043
Jan–Mar	0.2361	0.0437	0.0209	0.0470	0.1166	0.0010	0.0047
Apr–Jun	0.0958	0.0196	0.0182	0.0246	0.1579	0.0014	0.0073
Jul–Sept	0.1066	0.0189	0.0342	0.0809	0.0794	0.0019	0.0038
Oct–Dec	0.0953	0.0117	0.0392	0.0993	0.1184	0.0028	0.0047
Averaged	0.1141	0.0213	0.0272	0.0613	0.1116	0.0015	0.0049
			DDRM PSD in 1 km × 1 km				
Annual	0.0109	0.0627	0.0775	0.0446	0.0468	0.0037	0.0002
Jan–Mar	0.0125	0.0385	0.0860	0.0393	0.0601	0.0099	0.0048
Apr–Jun	0.0026	0.0565	0.0798	0.0453	0.0507	0.0076	0.0039
Jul–Sept	0.0786	0.0214	0.0764	0.0343	0.0605	0.0069	0.0040
Oct–Dec	0.0182	0.0900	0.0838	0.0402	0.0562	0.0091	0.0040
Averaged	0.0246	0.0538	0.0807	0.0407	0.0549	0.0074	0.0034

Table 10. The q statistics of the different driving factors on the spatial distribution of ESA CCI and the DDRM profile saturation degree (PSD) temporal averages of the YR catchment in the geographical detector method.

	PRE	NDVI	LUCC	DEM	ST	SL	AS
			ESA CCI PSD in 1 km × 1 km				
Annual	0.0674	0.0694	0.0700	0.2966	0.1348	0.0001	0.0132
Jan–Mar	0.3622	0.0382	0.0780	0.3341	0.1477	0.0004	0.0120
Apr–Jun	0.1059	0.1102	0.0986	0.3943	0.1773	0.0006	0.0113
Jul–Sept	0.0795	0.0456	0.0522	0.2333	0.1149	0.0003	0.0163
Oct–Dec	0.1806	0.0247	0.0461	0.1982	0.0801	0.0002	0.0096
Averaged	0.1591	0.0576	0.0690	0.2913	0.1309	0.0003	0.0125
			DDRM PSD in 1 km × 1 km				
Annual	0.0033	0.0107	0.0111	0.0806	0.0155	0.0006	0.0005
Jan–Mar	0.0427	0.0168	0.0504	0.1771	0.0486	0.0021	0.0009
Apr–Jun	0.0055	0.0186	0.0187	0.0883	0.0197	0.0015	0.0005
Jul–Sept	0.0265	0.0022	0.0031	0.0413	0.0058	0.0003	0.0025
Oct–Dec	0.0882	0.0116	0.0224	0.0559	0.0197	0.0006	0.0022
Averaged	0.0332	0.0120	0.0211	0.0886	0.0218	0.0010	0.0013

5. Discussion

5.1. The Limitations and Uncertainties Associated with the Datasets

This study chooses the European Space Agency Climate Change Initiative (ESA CCI) surface soil moisture product as the original data from satellite instruments and the DEM-based distributed rainfall-runoff model (DDRM) to provide profile soil moisture data simulated from hydrological models. In order to improve the reliability of PSM datasets acquired from DDRM, the model was calibrated by using the observed runoff from 2014–2016 and was verified by the observed runoff from 2017. However, there are still limitations and uncertainties associated with the datasets. For DDRM-simulated PSM datasets, the accuracy of the PSM is limited by the uncertainties of input data (precipitation and evapotranspiration), the model structure, and model parameters. Some previous papers have changed the input data, model parameters, and model structures to investigate

the uncertainties of the hydrological model simulations, including streamflow and soil moisture simulations [2,39,47,48]. In future studies, hydrological models with different model styles and structures can be considered to produce different hydrologically modeled PSM datasets for spatial heterogeneity investigations. Moreover, the spatial interpolation method used for the input data may affect the spatial pattern of the model-simulated PSM. In order to analyze the influence of the interpolation method, the model performance of streamflow and soil moisture simulations using the Kriging method to interpolate the input data was compared to the model performance using the IDW method, and the results indicate that the influence of the spatial interpolation method on both the temporal and spatial patterns of streamflow and soil moisture is low. This may be because hydrological modeling has the ability to adjust itself through model calibration.

For the PSM datasets acquired from the ESA CCI product, the accuracy of the data is limited by the uncertainties of raw satellite observations, retrieval algorithms, and preprocessing methods used in the study. For instance, the resampling of ESA CCI data from 25 km × 25 km to 1 km × 1 km introduces uncertainties in the spatial heterogeneity of the data; the constant value of CT applied in the exponential filter to transform SSM to PSM also introduces uncertainties since the CT values are affected by the topography, climatic conditions, vegetation types, soil types, etc. [49]. Because of the lack of in situ observations of profile soil moisture, only an indirect way (through model calibration and comparison of PSM with each other) is used to show that the data acquired from ESA CCI and DDRM contain some useful spatial information; there is no direct way to verify if the spatial datasets used in the study are correct. In situ observation networks can be set up and used as a third source, along with the validation criteria of profile soil moisture in future studies.

5.2. The Pros and Cons Associated with the Methods

This study uses the spatial statistical analysis and the semi-variogram method to identify the spatial heterogeneity of PSM acquired from different sources and uses the geographic detector method to seek out their driving factors. There are papers that analyze the driving factors of hydrological or meteorological factors by selecting the different input data of simple statistical models or conceptual models [50,51]. In these papers, the driving factors are determined according to the model structure, but the actual driving factors may be more complex and implicit. In the study, the input data (precipitation and evapotranspiration) of DDRM and the values of the model parameters can be changed to see their influence on the spatial distribution of DDRM PSM, but there are only two driving factors with explicit physical meanings that have been considered since the influential factors and physical meanings of the model parameters are ambiguous. Moreover, changing input data and model parameters would reduce the reliability of PSM simulations since it reduces the model performance of streamflow simulations, which means the simulation of the rainfall-runoff processes in DDRM would be less reliable. For ESA CCI PSM, the CT values can be changed to see the influence on the spatial distribution of ESA CCI PSM, but it is hard to distinguish the actual driving factors since there are many influential factors from CT values. Thus, this study chooses to analyze the PSM datasets acquired from ESA CCI and DDRM directly to see their spatial heterogeneity and corresponding driving factors rather than select different options to produce different datasets to seek out their driving factors.

The spatial statistical analysis and the semi-variogram method are both used to identify the spatial heterogeneity of PSM in the study since their results can complement and verify each other. When compared to the spatial heterogeneity of PSM, the limitation of the spatial statistical analysis is that the results are qualitative, not quantitative, and the limitation of the semi-variogram method is that the results are largely affected by scale effects. For the geographic detector method, the choices of the candidate driving factors and the method used to discretize the data both affect the results. In future studies, more candidate driving

factors and different discretizing methods can be considered to investigate their influences on the spatial heterogeneity of PSM.

6. Conclusions

In this study, the profile soil moisture (PSM) acquired based on European Space Agency Climate Change Initiative (ESA CCI) soil moisture products and the DEM-based distributed rainfall-runoff model (DDRM) are used to investigate the spatial heterogeneity and the driving factors of PSM. Three catchments were chosen as the study area, including two humid catchments, the Qu River (QR) catchment and Nanpan River (NR) catchment, and one semi-arid catchment, the Yiluo River (YR) catchment. By considering the scale dependence of spatial heterogeneity, the ESA CCI and DDRM profile saturation degree (PSD) datasets that match in terms of spatial scale and physical properties were acquired by first using satellite raw product preprocessing and hydrologically modeling; then, the spatial heterogeneity and driving factors were identified by using spatial statistical analysis, the semi-variogram method, and the geographic detector method. The results were comparatively analyzed, and the conclusions are summarized here:

(1) ESA CCI and DDRM PSD are similar for seasonal changes and are overall consistent and locally different in terms of spatial variations;
(2) Based on spatial statistical analysis, the spatial heterogeneity of PSD reduces after spatial rescaling; in the same spatial scale, DDRM PSD shows higher spatial heterogeneity than ESA CCI PSD, and the low-flow period shows higher spatial heterogeneity than the high-flow period;
(3) Based on the semi-variogram method, both ESA CCI PSD and DDRM PSD show strong spatial heterogeneity in different seasons, different spatial scales, and different catchments, in which the proportion of $C/(C_0 + C)$ is higher than 0.75, and the spatial data in the low-flow period mostly show larger spatial heterogeneity than that in the high-flow period, in which the proportion is higher than 0.9; the PSD in the YR catchment shows the largest spatial heterogeneity, and that in the QR catchment shows relatively low spatial heterogeneity;
(4) The first three driving factors of the spatial heterogeneity of both ESA CCI and DDRM profile soil moisture are DEM, precipitation, and soil type in most cases, contributing more than 50% to spatial heterogeneity;
(5) Precipitation contributes most to ESA CCI PSD in the low-flow period when there is no obvious high contribution of precipitation to DDRM PSD.

This study provides insights into the potential mechanisms and differences of satellite-based and hydrologically modeled spatial profile soil moisture, which can help develop the refined modeling and spatial management strategies of soil moisture in ecological, agricultural, and hydrological fields. In future studies, spatial heterogeneity and the potential influential mechanism of combined, remotely sensed, and hydrologically modeled profile soil moisture can be investigated through data fusion or assimilation.

Author Contributions: Conceptualization, H.Y. and X.Z.; Formal analysis, H.Y.; Funding acquisition, H.Y. and Z.Y.; Investigation, H.Y.; Methodology, H.Y. and X.Z.; Project administration, H.Y. and Z.Y.; Resources, H.Y. and Z.Y.; Supervision, Z.Y., B.X. and J.H.; Validation, X.Z. and B.X.; Writing—original draft, H.Y.; Writing—review & editing, X.Z. and Z.Y. All authors have read and agreed to the published version of the manuscript.

Funding: This research was funded by the National Natural Science Foundation of China, grant number 52209007, the National Natural Science Foundation of China, grant number U2340208, the Natural Science Foundation of Hubei Province, grant number 2022CFD037, the Fundamental Research Funds for Central Public Welfare Research Institutes, grant number CKSF2023295/SZ.

Data Availability Statement: The data presented in this study are available on request from the corresponding author. The data are not publicly available due to privacy.

Conflicts of Interest: The authors declare no conflict of interest.

References

1. Pal, M.; Maity, R. Assimilation of remotely sensed based surface soil moisture to develop a spatially varying vertical soil moisture profile database for entire Indian mainland. *J. Hydrol.* **2021**, *601*, 126807. [CrossRef]
2. Yang, H.; Xiong, L.; Liu, D.; Cheng, L.; Chen, J. High spatial resolution simulation of profile soil moisture by assimilating multi-source remote-sensed information into a distributed hydrological model. *J. Hydrol.* **2021**, *597*, 126311. [CrossRef]
3. Brakhasi, F.; Walker, J.P.; Ye, N.; Wu, X.; Shen, X.; Yeo, I.Y.; Boopathi, N.; Kim, E.; Kerr, Y.; Jackson, T. Towards soil moisture profile estimation in the root zone using L- and P-band radiometer observations: A coherent modelling approach. *Sci. Remote Sensed* **2023**, *7*, 100079. [CrossRef]
4. Dai, A.; Trenberth, K.E.; Qian, T. A global dataset of palmer drought severity index for 1870–2002: Relationship with soil moisture and effects of surface warming. *J. Hydrometeorol.* **2004**, *5*, 1117–1130. [CrossRef]
5. Suseela, V.; Conant, R.T.; Wallenstein, M.D.; Dukes, J.S. Effects of soil moisture on the temperature sensitivity of heterotrophic respiration vary seasonally in an old-field climate change experiment. *Glob. Chang. Biol.* **2015**, *18*, 336–348. [CrossRef]
6. Humphrey, V.; Berg, A.; Ciais, P.; Gentine, P.; Frankenberg, C. Soil moisture–atmosphere feedback dominates land carbon uptake variability. *Nature* **2021**, *592*, 65–69. [CrossRef] [PubMed]
7. Koster, R.D.; Dirmeyer, P.A.; Guo, Z.; Bonan, G.; Chan, E.; Cox, P.; Yamada, T. Regions of strong coupling between soil moisture and precipitation. *Science* **2004**, *305*, 1138–1140. [CrossRef] [PubMed]
8. Dorigo, W.A.; Wagner, W.; Hohensinn, R.; Hahn, S.; Paulik, C.; Xaver, A.; Jackson, T. The International Soil Moisture Network: A data hosting facility for global in situ soil moisture measurements. *Hydrol. Earth Syst. Sci.* **2011**, *15*, 1675–1698. [CrossRef]
9. Green, J.K.; Seneviratne, S.I.; Berg, A.M.; Findell, K.L.; Hagemann, S.; Lawrence, D.M.; Gentine, P. Large influence of soil moisture on long-term terrestrial carbon uptake. *Nature* **2019**, *565*, 476–479. [CrossRef]
10. Lal, P.; Shekhar, A.; Gharun, M.; Das, N.N. Spatiotemporal evolution of global long-term patterns of soil moisture. *Sci. Total Environ.* **2023**, *867*, 161470. [CrossRef]
11. An, R.; Zhang, L.; Wang, Z.; Quaye-Ballard, J.A.; You, J.; Shen, X.; Gao, W.; Huang, L.; Zhao, Y.; Ke, Z. Validation of the ESA CCI soil moisture product in China. *Int. J. Appl. Earth Obs. Geoinf.* **2016**, *48*, 28–36. [CrossRef]
12. Zhang, L.; Liu, Y.; Ren, L.; Jiang, S.; Yang, X.; Yuan, F.; Wei, L. Drought Monitoring and Evaluation by ESA CCI Soil Moisture Products over the Yellow River Basin. *IEEE J. Sel. Top. Appl. Earth Obs. Remote. Sensed* **2019**, *12*, 3376–3386. [CrossRef]
13. Montenbruck, O.; Gill, E.; Lutze, F. Satellite orbits: Models, methods, and applications. *Appl. Mech. Rev.* **2002**, *55*, B27–B28. [CrossRef]
14. Srivastava, P.K. Satellite soil moisture: Review of theory and applications in water resources. *Water Resour. Manag.* **2017**, *31*, 3161–3176. [CrossRef]
15. Sheffield, J.; Wood, E.F.; Pan, M.; Beck, H.; Coccia, G.; Serrat-Capdevila, A.; Verbist, K. Satellite remotely sensed for water resources management: Potential for supporting sustainable development in data-poor regions. *Water Resour. Res.* **2018**, *54*, 9724–9758. [CrossRef]
16. Kodheli, O.; Lagunas, E.; Maturo, N.; Sharma, S.K.; Shankar, B.; Montoya, J.F.M.; Duncan, J.C.M.; Spano, D.; Chatzinotas, S.; Kisseleff, S.; et al. Satellite communications in the new space era: A survey and future challenges. *IEEE Commun. Surv. Tutor.* **2020**, *23*, 70–109. [CrossRef]
17. Liu, Y.Y.; Dorigo, W.A.; Parinussa, R.M.; de Jeu, R.A.M.; Wagner, W.; McCabe, M.F.; Evans, J.P.; van Dijk, A.I.J.M. Trend-preserving blending of passive and active microwave soil moisture retrievals. *Remote. Sensed Environ.* **2012**, *123*, 280–297. [CrossRef]
18. Al-Yaari, A.; Wigneron, J.P.; Dorigo, W.; Colliander, A.; Pellarin, T.; Hahn, S.; Mialon, A.; Richaume, P.; Fernandez-Moran, R.; Fan, L.; et al. Assessment and inter-comparison of recently developed/reprocessed microwave satellite soil moisture products using ISMN ground-based measurements. *Remote. Sensed Environ.* **2019**, *224*, 289–303. [CrossRef]
19. Kim, H.; Wigneron, J.P.; Kumar, S.; Dong, J.; Wagner, W.; Cosh, M.H.; Bosch, D.D.; Collins, C.H.; Starks, P.J.; Seyfried, M.; et al. Global scale error assessments of soil moisture estimates from microwave-based active and passive satellites and land surface models over forest and mixed irrigated/dryland agriculture regions. *Remote. Sensed Environ.* **2020**, *251*, 112052. [CrossRef]
20. Martens, B.; Miralles, D.G.; Lievens, H.; Van Der Schalie, R.; De Jeu, R.A.; Fernández-Prieto, D.; Beck, H.E.; Dorigo, W.A.; Verhoest, N.E. GLEAM v3: Satellite-based land evaporation and root-zone soil moisture. *Geosci. Model Dev.* **2017**, *10*, 1903–1925. [CrossRef]
21. Xing, Z.; Fan, L.; Zhao, L.; De Lannoy, G.; Frappart, F.; Peng, J.; Li, X.; Zeng, J.; AI-Yaari, A.; Yang, K.; et al. A first assessment of satellite and reanalysis estimates of surface and root-zone soil moisture over the permafrost region of Qinghai-Tibet Plateau. *Remote. Sensed Environ.* **2021**, *265*, 112666. [CrossRef]
22. Zhao, R.J. The Xinanjiang model applied in China. *J. Hydrol.* **1992**, *135*, 371–381. [CrossRef]
23. Christofides, P.D.; Scattolini, R.; de la Pena, D.M.; Liu, J. Distributed model predictive control: A tutorial review and future research directions. *Comput. Chem. Eng.* **2013**, *51*, 21–41. [CrossRef]
24. Devia, G.K.; Ganasri, B.P.; Dwarakish, G.S. A review on hydrological models. *Aquat. Procedia* **2015**, *4*, 1001–1007. [CrossRef]
25. Lei, F.; Crow, W.T.; Shen, H.; Su, C.H.; Holmes, T.R.; Parinussa, R.M.; Wang, G. Assessment of the impact of spatial heterogeneity on microwave satellite soil moisture periodic error. *Remote. Sensed Environ.* **2018**, *205*, 85–99. [CrossRef] [PubMed]
26. Zhang, E.; Liu, Y.; Pan, T.; Tan, Q.; Ma, Z. Evaluating the Effects of Climate Change and Human Activities on the Seasonal Trends and Spatial Heterogeneity of Soil Moisture. *Remote. Sensed* **2022**, *14*, 4862. [CrossRef]
27. Yang, Y.; Dou, Y.; Liu, D.; An, S. Spatial pattern and heterogeneity of soil moisture along a transect in a small catchment on the Loess Plateau. *J. Hydrol.* **2017**, *550*, 466–477. [CrossRef]

28. Zhang, Z.; Yin, H.; Zhao, Y.; Wang, S.; Han, J.; Yu, B.; Xue, J. Spatial heterogeneity and driving factors of soil moisture in alpine desert using the geographical detector method. *Water* **2021**, *13*, 2652. [CrossRef]
29. Preimesberger, W.; Scanlon, T.; Su, C.-H.; Gruber, A.; Dorigo, W. Homogenization of Structural Breaks in the Global ESA CCI Soil Moisture Multisatellite Climate Data Record. *IEEE Trans. Geosci. Remote. Sensed* **2021**, *59*, 2845–2862. [CrossRef]
30. Gruber, A.; Scanlon, T.; van der Scalie, R.; Wagner, W.; Dorigo, W. Evolution of the ESA CCI Soil Moisture climate data records and their underlying merging methodology. *Earth Syst. Sci. Data* **2019**, *11*, 717–739. [CrossRef]
31. Dorigo, W.; Wagner, W.; Albergel, C.; Albrecht, F.; Balsamo, G.; Brocca, L.; Haas, E. ESA CCI Soil Moisture for improved Earth system understanding: State-of-the art and future directions. *Remote. Sensed Environ.* **2017**, *203*, 185–215. [CrossRef]
32. Liu, Y.Y.; Parinussa, R.M.; Dorigo, W.A.; De Jeu, R.A.; Wagner, W.; Van Dijk, A.I.J.M.; McCabe, M.F.; Evans, J.P. Developing an improved soil moisture dataset by blending passive and active microwave satellite-based retrievals. *Hydrol. Earth Syst. Sci.* **2011**, *15*, 425–436. [CrossRef]
33. Papagiannopoulou, C.; Miralles, D.G.; Dorigo, W.A.; Verhoest, N.E.C.; Depoorter, M.; Waegeman, W. Vegetation anomalies caused by antecedent precipitation in most of the world. *Environ. Res. Lett.* **2017**, *12*, 074016. [CrossRef]
34. Hargreaves, G.H.; Samani, Z.A. Estimating potential evapotranspiration. *J. Irrig. Drain. Div.* **1982**, *108*, 225–230. [CrossRef]
35. Tomczak, M. Spatial interpolation and its uncertainty using automated anisotropic inverse distance weighting (IDW)-cross-validation/jackknife approach. *J. Geogr. Inf. Decis. Anal.* **1998**, *2*, 18–30.
36. Chen, S.; Xiong, L.; Zeng, L.; Kim, J.S.; Zhang, Q.; Jiang, C. Distributed rainfall-runoff simulation for a large-scale karst catchment by incorporating landform and topography into the DDRM model parameters. *J. Hydrol.* **2022**, *610*, 127853. [CrossRef]
37. Xiong, L.; Guo, S.L.; Tian, X.R. DEM-based distributed hydrological model and its application. *Adv. Water Sci.* **2004**, *15*, 517–520. (In Chinese)
38. Xiong, L.; Yang, H.; Zeng, L.; Xu, C.Y. Evaluating Consistency between the Remote-sensed Soil Moisture and the Hydrological Model-Simulated Soil Moisture in the Qujiang Catchment of China. *Water* **2018**, *10*, 291. [CrossRef]
39. Yang, H.; Xiong, L.; Ma, Q.; Xia, J.; Chen, J.; Xu, C.Y. Utilizing Satellite Surface Soil Moisture Data in Calibrating a Distributed Hydrological Model Applied in Humid Regions Through a Multi-Objective Bayesian Hierarchical Framework. *Remote. Sensed* **2019**, *11*, 1335. [CrossRef]
40. Gill, M.A. Flood routing by the Muskingum method. *J. Hydrol.* **1978**, *36*, 353–363. [CrossRef]
41. Nash, J.E.; Sutcliffe, J.V. River flow forecasting through conceptual models part I—A discussion of principles. *J. Hydrol.* **1970**, *10*, 282–290. [CrossRef]
42. Wagner, W.; Lemoine, G.; Rott, H. A method for estimating soil moisture from ERS scatterometer and soil data. *Remote. Sensed Environ.* **1999**, *70*, 191–207. [CrossRef]
43. Isaaks, E.H.; Srivastava, R.M. *Applied Geostatistics*, *561*; Oxford University Press: New York, NY, USA, 1989.
44. Wang, J.; Li, X.; Christakos, G.; Liao, Y.; Zhang, T.; Gu, X.; Zheng, X. Geographical detectors-based health risk assessment and its application in the neural tube defects study of the Heshun region, China. *Int. J. Geogr. Inf. Sci.* **2010**, *24*, 107–127. [CrossRef]
45. Zhang, Y.; Zhang, K.C.; An, Z.S.; Yu, Y.P. Quantification of driving factors on NDVI in oasis-desert ecotone using geographical detector method. *J. Mt. Sci.* **2019**, *16*, 2615–2624. [CrossRef]
46. Chen, J.; Yang, S.T.; Li, H.W.; Zhang, B.; Lv, J.R. Research on geographical environment unit division based on the method of natural breaks (Jenks). *Int. Arch. Photogramm. Remote Sens. Spat. Inf. Sci.* **2013**, *40*, 47–50. [CrossRef]
47. Liu, Y.; Gupta, H.V. Uncertainty in hydrologic modeling: Toward an integrated data assimilation framework. *Water Resour. Res.* **2007**, *43*, W07401. [CrossRef]
48. Schreiner-McGraw, A.P.; Ajami, H. Impact of uncertainty in precipitation forcing data sets on the hydrologic budget of an integrated hydrologic model in mountainous terrain. *Water Resour. Res.* **2020**, *56*, e2020WR027639. [CrossRef]
49. Sutanudjaja, E.H.; Van Beek, L.P.H.; De Jong, S.M.; Van Geer, F.C.; Bierkens, M.F.P. Calibrating a large-extent high-resolution coupled groundwater-land surface model using soil moisture and discharge data. *Water Resour. Res.* **2014**, *50*, 687–705. [CrossRef]
50. Yang, H.; Xiong, L.; Xiong, B.; Zhang, Q.; Xu, C.Y. Separating runoff change by the improved Budyko complementary relationship considering effects of both climate change and human activities on basin characteristics. *J. Hydrol.* **2020**, *591*, 125330. [CrossRef]
51. Wu, J.; Miao, C.; Wang, Y.; Duan, Q.; Zhang, X. Contribution analysis of the long-term changes in seasonal runoff on the Loess Plateau, China, using eight Budyko-based methods. *J. Hydrol.* **2017**, *545*, 263–275. [CrossRef]